

REGULAR PAPER

# Derivation of control inputs for deep stall recovery using nonlinear frequency analysis

D. H. Nguyen<sup>\*</sup>, M. H. Lowenberg and S. A. Neild

Department of Aerospace Engineering, University of Bristol, Bristol, UK

\*Corresponding author email: [duc.nguyen@bristol.ac.uk](mailto:duc.nguyen@bristol.ac.uk)

**Received:** 8 October 2021; **Revised:** 7 April 2022; **Accepted:** 7 April 2022

**Keywords:** Deep stall; Frequency response; Bifurcation analysis; Flight dynamics; T-tail; dynamical systems

## Abstract

Although the problem of locked-in deep stall is well documented over many years, there currently exists no consistent procedure that can guarantee recovery. Past studies have suggested that it might be possible to rock the aircraft in pitch to destabilise the statically stable deep stall trim point, thereby gaining enough momentum to push the nose down. However, the methods used in these studies are either of preliminary or empirical nature and cannot guarantee recovery. In this paper, we use bifurcation analysis to derive a recovery manoeuvre, specifically by assessing the aircraft's nonlinear frequency response under an elevator forcing. The ensuing nonlinear Bode plot detects unstable (divergent) solutions near resonance that contribute to a successful deep stall recovery. Moreover, the nonlinear resonant frequency is slightly lower than the result obtained using linear analysis, and time simulation shows that relying on the linear result does not lead to a successful recovery. It is also found that at the high angles of attack associated with deep stall, the frequency separation between the short period and phugoid mode is significantly reduced, leading to only one visible peak in the frequency response. This feature is also reflected in the time-domain step response.

## Nomenclature

$A$	forcing amplitude (deg)
$C_l, C_m, C_n$	total body-axes rolling, pitching, and yawing moment coefficients
$C_x, C_y, C_z$	total body-axes force coefficients
$p, q, r$	body-axis roll, pitch, and yaw rates (deg/s)
$t$	time (s)
$V$	velocity (m/s)
$Y$	general y-coordinate
$\alpha$	angle-of-attack (deg)
$\beta$	sideslip angle (deg)
$\delta_e, \delta_a$	elevator and aileron deflections (deg)
$\theta$	pitch angle (deg)
$\omega$	forcing frequency (rad/s)
$\phi$	bank angle (deg)

## 1.0 Introduction

Deep stall (also known as super stall) is a dangerous phenomenon in which the aircraft is locked into a high angle-of-attack attitude that results in a steep descending trajectory, despite a full nose-down input from the pilot. It is known that the following features can make an aircraft more susceptible to a deep stall:

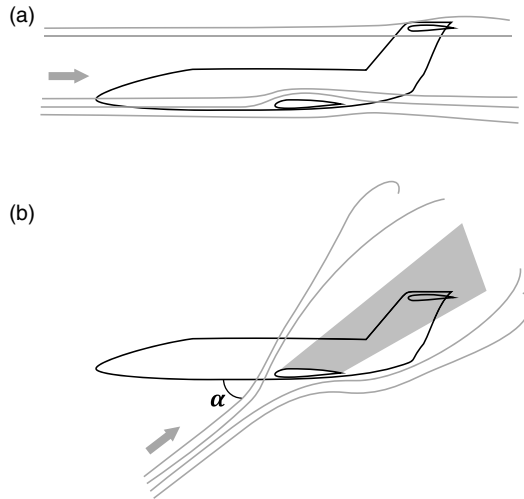


Figure 1. A T-tail aircraft in (a) normal flight (b) and deep stall.

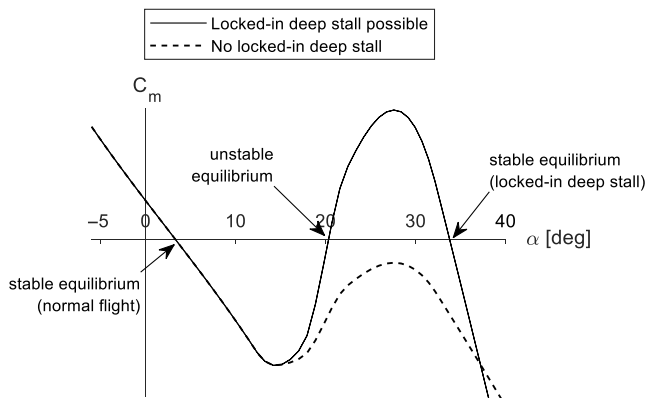


Figure 2. Typical pitching moment coefficient plot for the T-tail configuration. Negative slope indicates positive static stability in pitch.

- A T-tail configuration, for which the airflow at the elevator and tailplane is blocked by the wing/fuselage wake at high angles of attack, rendering them ineffective (see Fig. 1).
- An aft centre of gravity, which reduces the elevator/tailplane moment arm. This feature is usually found in statically unstable fighter aircraft for improved manoeuvrability, controllability in the presence of shock waves and reduced trim drag. Consideration of centre of gravity movement is also relevant in terms of ensuring safe flight of an airliner over the full range of possible loading conditions.

A deep stall can be predicted by examining the pitching moment coefficient plot such as the one shown in Fig. 2, specifically by locating the stable trim points ( $C_m = 0$ ) with negative slopes at high angles of attack. This information can be used to design safety devices that prevent the aircraft from excusing into the deep stall region, most commonly stick shaker and stick pusher [1] and digital angle-of-attack limiter in full-authority fly-by-wire systems [2, 3]. Nevertheless, research into deep stall recovery has not attracted much attention. Some past studies have highlighted a ‘dynamic recovery’ technique, which involves rocking the aircraft in pitch at or near a natural rigid-body frequency (short-period). This

manoeuvre can potentially induce a large-amplitude oscillation, allowing the pilot to push the nose down past the critical angle-of-attack (see [4] at the 06:20 mark for a recorded example on a real flight). Past studies on this technique, however, either involve simplified (second-order) flight dynamics models [5–9] or empirical methods that require high pilot workload in order to observe and match the stick-pumping frequency with the aircraft's natural frequency [3, 10]. The high workload can be attributed to the fact that upon entering a deep stall, there is a limited window to observe the aircraft's transient motion and figure out an input frequency before the motion damps out [3]. Furthermore, when using a mathematical model to determine a suitable pilot response, the nonlinearities in the aerodynamic data and the equations of motion will also affect the frequency characteristics: Depending on how the aircraft entered the deep stall, the ensuing oscillation may have different and varying frequencies, therefore making it more challenging to observe the motion and provide an appropriate forcing term [11]. Relying on visual cues to devise an escape manoeuvre can therefore be hit or miss, especially when the psychological and physical stresses on the pilot are considered. Therefore, it is desirable to know if a particular stick pumping frequency will guarantee recovery – regardless of how the aircraft entered and responded to the deep stall (i.e. an open-loop-like approach that requires no active monitoring by the pilot or feedback signal to the flight control system).

The use of bifurcation analysis and continuation methods has proven to be a powerful tool for nonlinear flight dynamics analysis in the past four decades [12–15]. Recent developments in the field saw the use of a harmonic forcing function to generate a 'nonlinear Bode plot', which facilitates assessments of the non-stationary nonlinear elements like sub/super-harmonic resonances [16] and actuator rate limiting [17] while also providing information on resonance and stability – none of which is available in linear-based frequency analysis. In an earlier study on the frequency-domain dynamics of an unstable fighter aircraft model at high angles of attack, we discovered that a simple harmonic elevator input can lead to nonlinear resonances with diverging amplitudes [11]. This phenomenon destabilises the statically stable deep stall trim point, which allows the pilot to do the pitch rocking manoeuvre in an open-loop manner with a higher chance of recovery. The deep stall observed in [11] is caused by the aft centre-of-gravity position – commonly seen in high performance fighter jets – so the feasibility of the pitch rocking method on a T-tail aircraft has not been discussed.

Accordingly, this paper investigates the deep stall dynamics of an airliner model with a T-tail using both classical (linear-based) methods and harmonically forced bifurcation analysis. The flying qualities in the deep stall regime are discussed in depth, followed by an evaluation of the aircraft's responses in the frequency domain near resonance using nonlinear analysis. Our discussion focuses on how these nonlinear characteristics can be exploited during the pitch rocking manoeuvre and ensure recovery from a locked-in deep stall. Furthermore, we show that for the GTT, this method of escaping a deep stall is immune to aerodynamic symmetries while also being safer than relying on lateral-directional perturbation, which can potentially send the aircraft into dangerous upsets and loss-of-control situations [18, 19]. The discussion on the flying qualities at such high angles of attack is also relevant to researchers working on small unmanned aerial vehicles (UAVs) because there are various studies on deliberately bringing the UAV into a deep stall to minimise landing distance (i.e. a perched landing) [20–22]. Most of these small vehicles have enough pitch control authority to exit the deep stall flight regime. Nevertheless, it is known that a better understanding of the flying dynamics characteristics at such a high angle-of-attack is required to further refine the perched landing to operational level.

The aircraft model and the methods used in this study are described in sections 2 and 3. Section 4 presents the main result, followed by concluding remarks in section 5. All bifurcation analyses were done in the MATLAB/Simulink environment using the Dynamical Systems Toolbox [23], which is a MATLAB/Simulink implementation of the numerical continuation software AUTO [24].

## 2.0 Aircraft model

The NASA's Generic T-Tail Transport model (GTT) is used for this study – see Fig. 3. As the name suggests, this model represents a generic mid-size regional jet airliner with a T-tail configuration. Its



Figure 3. The NASA GTT.

aerodynamic data was collected from a series of low-speed sub-scale wind tunnel and water tunnel tests, and some preliminary studies have been reported in recent conferences [25–27]. Computational fluid dynamics simulations were also done by NASA to estimate the influence of Reynolds number on the measured aerodynamic data, allowing corrections to the pitching moment and pitch damping data to be implemented to represent the equivalent full-scale aircraft. These Reynolds-corrected data was used here to construct a fourth-order (longitudinal) model and an eighth-order (6 degrees of freedom) model without flaps and spoilers, which are deemed adequate for our purpose. In the fourth-order implementation, the model contains aerodynamics tables that are 1D and 2D functions of angle-of-attack and  $\alpha$ /elevator deflections. Pitch control is achieved by moving the elevator and/or the all-moving horizontal tailplane. The latter is fixed at full nose-up (–10 deg) in this study to facilitate the most serious locked-in deep stall conditions, which can be encountered during a runaway trim. Aerodynamic data is valid for angles of attack between –8° and 60°.

Using standard flight dynamics notations and sign conventions, the fourth-order longitudinal equations of motions are

$$\dot{\alpha} = \frac{1}{mV} \left[ \frac{1}{2} \rho V^2 S (C_x \cos \alpha - C_x \sin \alpha) - T \sin \alpha + mg \cos(\theta - \alpha) \right] + q \tag{1}$$

$$\dot{V} = \frac{1}{m} \left[ \frac{1}{2} \rho V^2 S (C_z \sin \alpha + C_x \cos \alpha) + T \cos \alpha - mg \sin(\theta - \alpha) \right] \tag{2}$$

$$\dot{q} = \frac{1}{2} \rho V^2 S c \frac{C_m}{I_y} - \frac{Th_e}{I_y} \tag{3}$$

$$\dot{\theta} = q \tag{4}$$

in which the coefficients of aerodynamic force along the body x and z axes  $C_x$  and  $C_z$  and the moment coefficient in pitch  $C_m$  are represented as follows:

$$C_i = C_{i_0}(\alpha) + C_{i_1}(\alpha, \delta_e) + C_{i_2}(\alpha) \frac{cq}{2V} \tag{5}$$

where  $i = [x, z, m]$ . The first, second and third coefficients in (5) reflect the contribution of the airframe, elevator deflection ( $\delta_e$ ), and aerodynamic damping, respectively. These coefficients are plotted in Fig. 4, and the remaining terms in (1-4) are constants listed in Table 1. We assume zero thrust for our analysis ( $T = 0$  N) due to the lack of an engine model for the GTT. This is a reasonable assumption because at

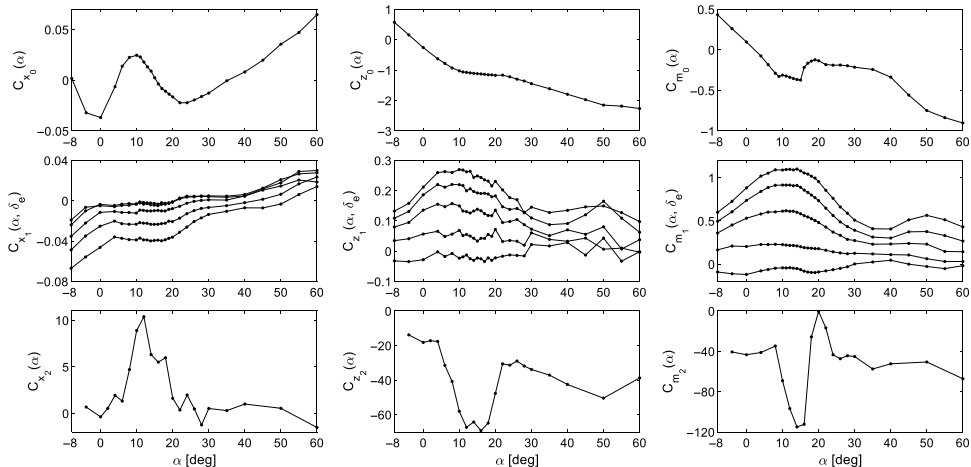


**Figure 4.** Aerodynamic coefficients at full nose-up tailplane.

the high angles of attack involved in a deep stall, any civil engines will be susceptible to significant performance degradation, so the zero thrust assumption corresponds to the worst-case scenario. This also ensures that no nose-down moment is generated by the high-mounted engines on the GTT, which can affect the outcomes concerning deep stall recovery.

It has been reported in [25] that a locked-in deep stall is possible when the centre of gravity is at 40% mean aerodynamic chord (MAC) and the horizontal tailplane is in full nose-down position ( $-10^\circ$ ). This is confirmed in Fig. 5, which shows a map of all the static trim points as functions of the elevator deflection ( $\delta_e$ ) projected onto three longitudinal states  $\alpha$  (angle-of-attack),  $V$  (velocity), and  $\theta$  (pitch angle). Stability of the trim solutions, obtained from local linearisation of the equations of motion, are indicated by line type. The diagram for pitch rate  $q$  is not shown in Fig. 5 since all equilibrium solutions have zero pitch rate. It can be seen that the stable deep stall branch at high angles of attack (above  $30^\circ$ ) extends all the way to  $\delta_e = 20^\circ$  – the maximum nose-down elevator position – which is indicative of a locked-in deep stall that agrees with sub-scale experimental results [25].

The existence of locked-in deep stall can be further explained by examining the values of pitching moment coefficient  $C_m$  against the angle-of-attack at different elevator positions (Fig. 6). For a deep stall around  $\alpha = 45^\circ$  (elevator close to neutral), there is nose-down elevator power available; but as the pilot or autopilot pushes the stick forward, the locked-in deep stall will move to a lower angle-of-attack ( $37^\circ$  at  $\delta_e = +20^\circ$ ). In this state, no further nose-down moment can be produced.

### 3.0 Nonlinear frequency response

Unlike the classical linear-based method, bifurcation analysis and numerical continuation can be used to generate the Bode plot of a nonlinear-harmonically forced system. This approach is implemented on the full nonlinear equations of motion (1-5), thereby allowing us to assess the dynamics without neglecting the contribution of the nonlinear terms as done in classical methods. The steps to implement bifurcation analysis on a nonlinear harmonically forced system are now presented. In general, the equations of motion must be written as autonomous first-order ordinary-differential equations. The harmonic forcing term  $\sin \omega t$  (or other equivalent) can be generated in such an environment by the addition of two ‘dummy states’  $x_5$  and  $x_6$  in the system:

$$\dot{x}_5 = x_5 + \omega x_6 - x_5 (x_5^2 + x_6^2) \quad (6)$$

**Table 1.** GTT parameters in Equations (1–4)

$c$	mean aerodynamic chord	3.37 m
$g$	gravitational acceleration	9.81 m/s <sup>2</sup>
$h_e$	thrust line distance above CG	2.02 m
$I_y$	pitch moment of inertia	1,510,624 kg/m <sup>2</sup>
$m$	mass	25,332 kg
$S$	wing area	70.1 m <sup>2</sup>
$T$	thrust	0 N
$\rho$	air density (at 10,000 ft)	0.905 kg/m <sup>3</sup>

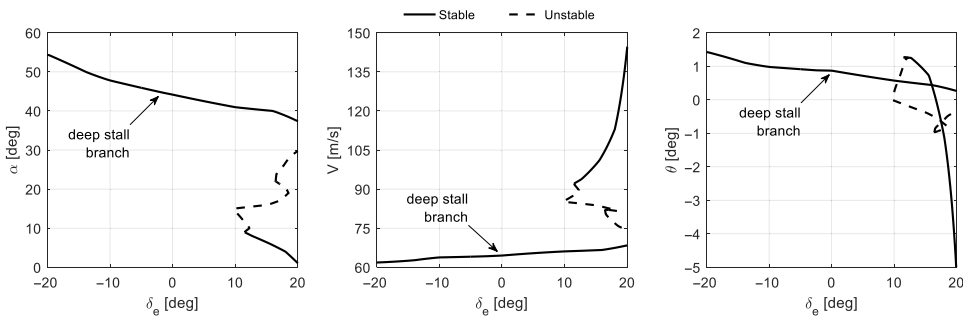


**Figure 5.** Static trim point map as function of elevator deflection (obtained using equilibrium bifurcation analysis). Assume zero thrust and full nose-up tailplane.

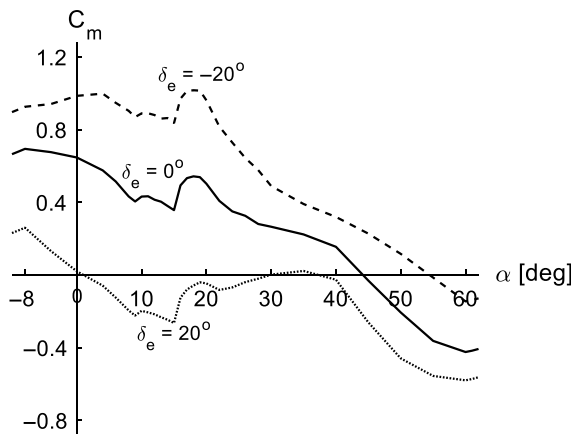


**Figure 6.** Pitching moment coefficients for three elevator positions at full nose-up tailplane.

$$\dot{x}_6 = -\omega x_5 + x_6 - x_6(x_5^2 + x_6^2) \tag{7}$$

It can be shown that  $x_5 = \sin \omega t$  and  $x_6 = \cos \omega t$  are asymptotically stable solutions of (6-7). We now couple the elevator input in equation (5) to the state  $x_5$

$$\delta_e = Ax_5 \tag{8}$$

giving  $\delta_e = A \sin \omega t$ , where  $A$  is the forcing amplitude in degree. The whole plant is now a sixth-order self-oscillating autonomous system, for which steady-state periodic solutions can be found by

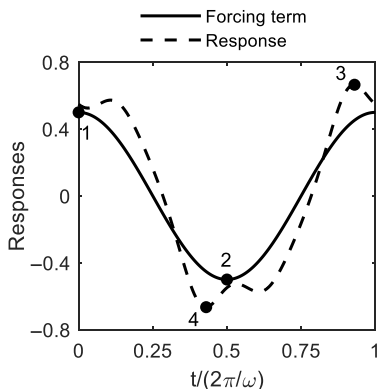


**Figure 7.** Example of a nonlinear harmonic solution obtained using continuation.

continuation in the same way as an autonomous (non-forced) system can be solved for limit-cycle solutions. The numerical continuation solver AUTO is used in this paper; details of its algorithm can be found in [28, 29].

An example of a non-sinusoidal response due to nonlinearities is shown in Fig. 7. To construct the nonlinear Bode diagram, we approximate the gain in dB as

$$\text{gain in dB} = 20 \log_{10} \left( \frac{Y_3 - Y_4}{Y_1 - Y_2} \right) \quad (9)$$

where  $Y_i$  refers to the y-coordinate of the point  $i$  in Fig. 7. Specifically, points 1 and 3 are the peaks and points 2 and 4 are the troughs. This method of analysing the frequency response of a nonlinear system tends to give identical results to the classical (linear) method when the forcing amplitude is small. In the pitch rocking manoeuvre, a large amplitude is almost certainly used, and this can result in a frequency response that differ significantly from its linear counterpart.

Stability information is provided by the continuation algorithm by analysing the Floquet multipliers – another feature that is not present in classical linear-based analysis. A periodic solution is marked as unstable when a Floquet multiplier crosses the unit circle. In this paper, the unstable solutions encountered result in large-amplitude oscillations that diverge to infinity. We consider this divergence a desirable feature for dynamic deep stall recovery.

It should be noted that because continuation only solves for the steady-state response, the Bode diagram (both linear and nonlinear) does not provide any indication of the transient dynamics, including how quickly the system converges to the steady-state solution observed on the Bode plot. We therefore do not discuss the phase relationship in the context of deep stall recovery. An understanding of this limitation is important when analysing the asymmetric full-order implementation of the GTT, as discussed in section 4.4.

## 4.0 Result and discussion

### 4.1 Frequency analysis: Linear

We begin our discussion by examining the changes in flying qualities when the aircraft is in a deep stall using classical methods. By linearising the GTT at  $5^\circ$  and  $44^\circ$  angles of attack – representing normal and deep stall conditions – we obtain two sets of state-space models listed in the appendix. Their frequency responses are plotted in Fig. 8. Two distinct features are noted:

- The deep stall frequency responses have lower gains across all four states, reflecting a considerable loss of pitch control authority at such a high angle-of-attack.

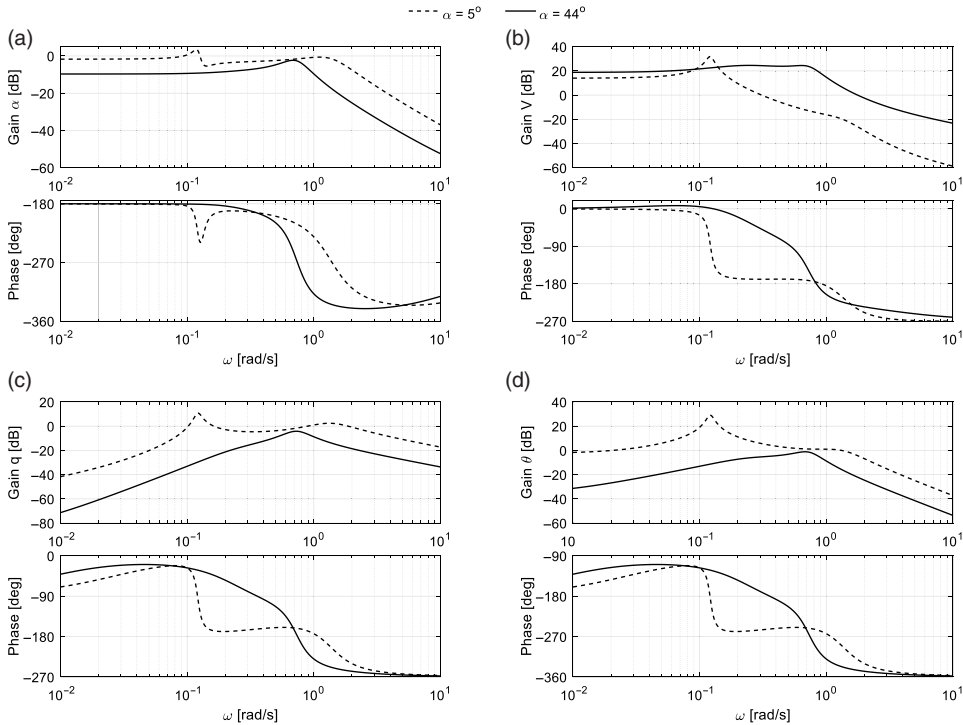


**Figure 8.** Linear frequency responses at normal flight ( $\alpha = 5^\circ$ ) and deep stall ( $\alpha = 44^\circ$ ) for all four longitudinal states. Natural frequencies at deep stall: 0.23 and 0.68 rad/s. The linear transfer functions are listed in the appendix.

- Only one apparent peak is visible in the deep stall frequency response as opposed to the two conventional phugoid and short period peaks at low angle-of-attack. This indicates that the frequency separation between those two modes is reduced in deep stall conditions.

The pole positions of these two sets of frequency responses are shown in Fig. 9. As the angle-of-attack increases, the short period and phugoid roots approach each other and reduce their frequency separation in the process. At  $44^\circ$  angle-of-attack, these two modes have frequencies that are of the same order of magnitude (0.23 and 0.68 rad/s) with almost identical damping, making them barely able to be discerned on the  $\alpha$  frequency response. The time-domain responses in Fig. 10 also reflect the unconventional dynamics: in the second plot, a single-mode-like response is observed as opposed to the distinctly visible short period and phugoid motions in the first plot. Therefore, any controller designed for normal flight will be much less effective in this deep stall region due to the unconventional dynamics that does not follow the traditional short-period and phugoid model, upon which the design of most controllers is based.

For future work, the transition to the ‘single-mode’ dynamics observed in the deep stall region can be studied using the eigenvector similarity metric outlined in reference [30], which is the first application of the method in a flight dynamics context. The insight gained from this methodology can improve our understanding of the flight dynamics at high angles of attack and potentially be used to aid controller design. The use of a fourth-order longitudinal model will also provide a simple example for demonstrating the eigenvector analysis framework because the test case provided in reference [30] involves lateral-directional coupling, which made the stall and post-stall upset behaviours more difficult to interpret.

To conclude, there is effectively one resonance frequency at deep stall, which is beneficial for the pitch rocking manoeuvre. If the pilot pumps the stick at this frequency, it may be possible to induce a large

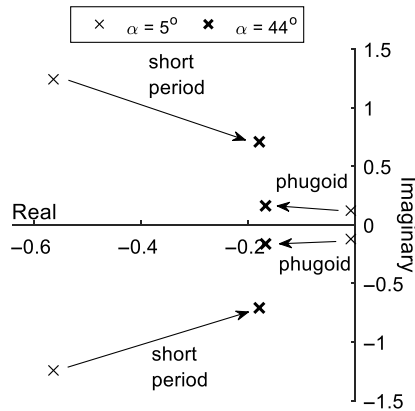


Figure 9. Pole positions: normal flight vs deep stall.

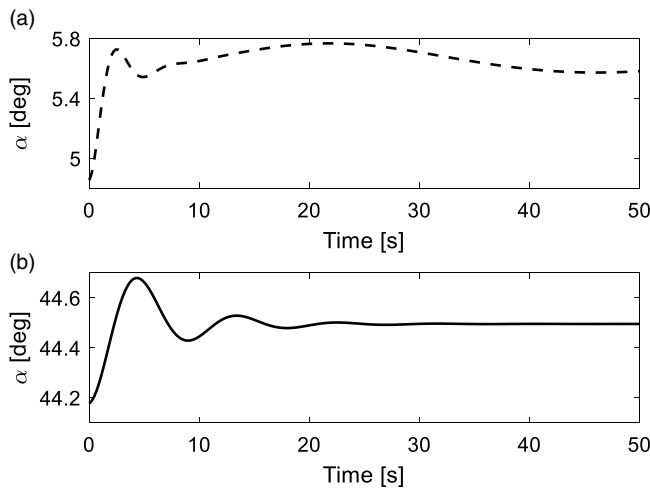
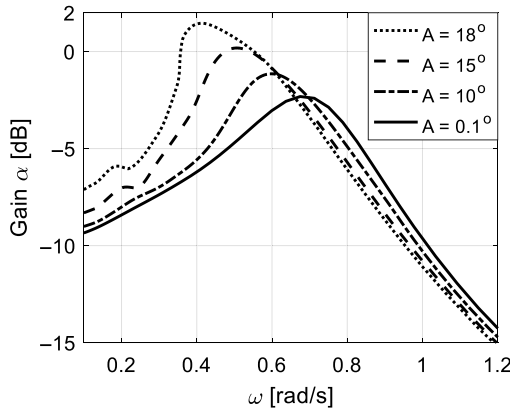


Figure 10. Nonlinear simulation of a  $1^\circ$  elevator step response in: (a) normal flight and (b) deep stall.

oscillation to push the nose down. The manoeuvre will almost certainly involve large stick movement. This is where the validity of linear-based analysis could be questioned since the method is only accurate locally (i.e. at a small forcing frequency). In the next section, nonlinear frequency analysis is employed to uncover further changes in dynamics at deep stall due to large-amplitude forcing and to help devise a successfully recovery manoeuvre.

#### 4.2 Frequency analysis: Nonlinear

Because the frequency responses of most nonlinear systems exhibit a dependency on the forcing amplitude, we first examine the impact of changing  $A$  in  $\delta_e = A \sin \omega t$  using continuation. Figure 11 shows that as  $A$  increases, the resonance peak (defined here as the point with the highest gain) increases in amplitude and moves to the left. These two phenomena are properties of a softening system, in which the stiffness reduces with increasing oscillation amplitude. In the context of dynamic deep stall recovery, this further validates the feasibility of the pitch rocking manoeuvre (stiffness reduces with increasing forcing amplitudes, thereby facilitating recovery) while also underlining the fact that the response is nonlinear. The movement of the resonance peak as a function of  $A$  up to  $18^\circ$  is illustrated in Fig. 12,



**Figure 11.** Nonlinear  $\alpha$ -to- $\delta_e$  frequency responses at different forcing amplitudes. All solutions are stable. The frequency response at  $A = 0.1^\circ$  is identical to the linear one.

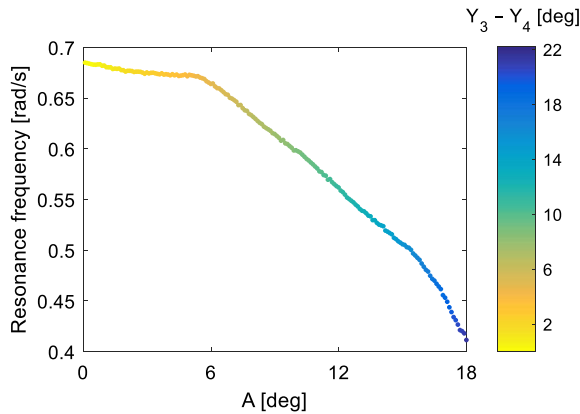


**Figure 12.** Impact of forcing amplitude on the frequency and gain at resonance of the  $\alpha$  frequency response. All solutions are stable.

noting that the colour reflects how much the oscillation deviates from the trim point at  $\alpha = 44^\circ$  (as in  $Y_3 - Y_4$  based on the definition in Fig. 7). It is evident that the amplitude dependency is strong, which causes the resonance frequency to reduce as the forcing amplitude increases.

The forcing amplitude is now further increased to 18.48 deg. Examining its frequency response in Fig. 13a shows that there has been a qualitative change in the system dynamics. Firstly, the resonance peak bends strongly to the left, creating a very small region where three solutions exist (two stable and one unstable). Secondly, an unstable isola (a separate family of solutions that is not connected to the main branch) was detected around the area. Increasing  $A$  further causes the isola to merge with the main branch as seen in Fig. 13b – noting that 20 deg is the maximum possible forcing amplitude for this aircraft model. At this stop-to-stop stick pumping amplitude, only unstable solutions exist between 0.29 and 0.51 rad/s, and forcing the aircraft at a frequency within this range leads to oscillations of growing amplitude that diverge to infinity.

To verify the stability information derived from continuation, we compare the time simulations of the aircraft forced at two different frequencies: 0.68 rad/s (the resonance frequency as predicted by linear analysis) and 0.40 rad/s (one of the unstable solutions at  $A = 20^\circ$ ). Figure 14 confirms that the forced response at 0.40 rad/s is divergent, which crashed the simulation after the 57s mark due to the ensuing

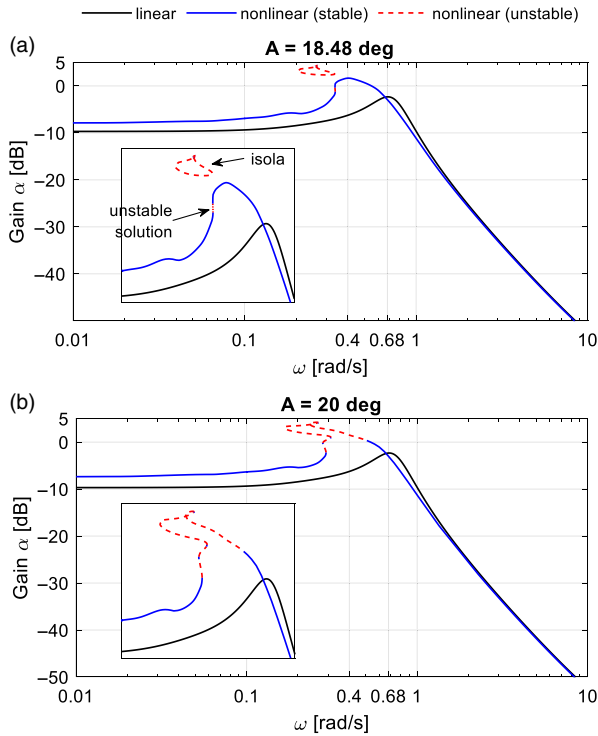


Figure 13.  $\alpha$  frequency responses at very large forcing amplitudes. Insets show magnified views.

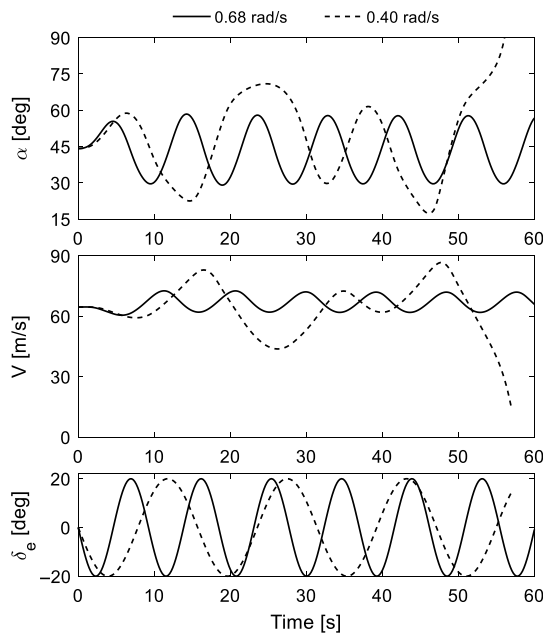
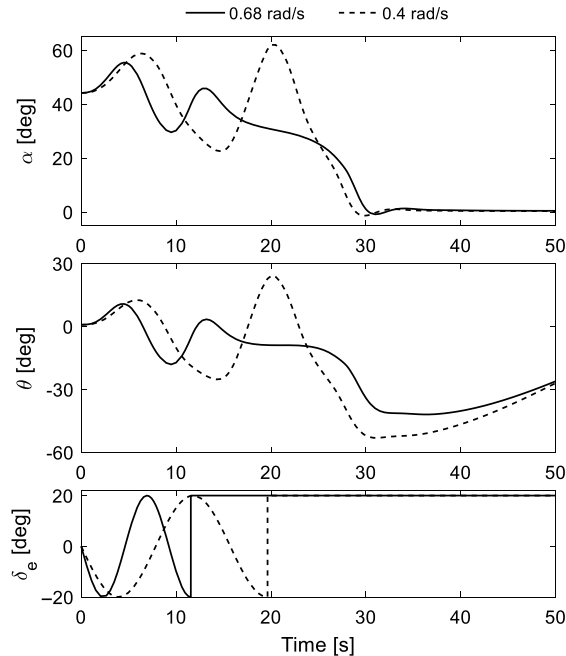


Figure 14. Forced responses.  $\delta_e = -20 \sin \omega t$  (deg).



**Figure 15.** Example recovery attempts.

large-amplitude oscillation. On the other hand, the response at the linear resonant frequency of 0.68 rad/s is verified to be stable and does not give the highest oscillation amplitude as suggested by the linear analysis. Large oscillations with growing amplitude like in the 0.40 rad/s case are beneficial for deep stall recovery because the aircraft can gain considerable momentum, making it easier to push the nose down and bring the angle-of-attack back to the low- $\alpha$  regime. The divergent response at 0.40 rad/s also causes large variation in the total velocity  $V$  as seen in Fig. 14 as well as in the pitch angle  $\theta$  (not shown). Therefore, it can be inferred that past studies that only considered the short-period dynamics and ignored variations in  $V$  and  $\theta$  [7–9] cannot accurately reflect the aircraft dynamics in this high- $\alpha$  regime, making them unsuitable for analysing dynamic deep stall recovery. It is also worth noting that no subharmonic resonance (additional peaks at low frequencies) is detected in the GTT frequency response, unlike in the unstable fighter jet example [11].

Finally, the movement of the resonance peak in Fig. 12 suggests that even when a divergent response cannot be achieved, such as when an actuator fault prevents the pilot from achieving stop-to-stop elevator travel (resulting in a frequency response resembling those shown in Fig. 11), a reasonably large oscillation can still occur with a good chance of recovery. The key point here is that the stick pumping frequency should be lower than the resonance frequency predicted by linear analysis.

### 4.3 Recovery procedure

It has been established using nonlinear frequency analysis that the resonance frequency at a large forcing amplitude is lower than the predicted value using linear analysis, and that the oscillation near resonance can be divergent. To leverage this phenomenon in a deep stall recovery, the pilot should pump the stick at a frequency in the unstable region to build up momentum, then push nose-down once the oscillation amplitude is large enough. Two example recovery attempts are presented in Fig. 15 using the two forcing frequencies discussed previously. In both cases, the pilot forces the aircraft for 1.25 cycles (initiated by a nose-up input), then applies a full nose-down elevator step at the top of the second nose-up pull. It can

be seen that the 0.40 rad/s forcing results in a much larger oscillation. When the nose-down step was applied, the angle-of-attack of the 0.40 rad/s response quickly ‘overtakes’ (having lower  $\alpha$ ) the 0.68 rad/s one at the 25s mark thanks to the large built-up momentum from the preceding harmonic forcing, despite the large 8s gap between their nose-down inputs. Both examples converge to the same low- $\alpha$  attitude at around the same time, but the time from nose-down input to recovery is far shorter in the 0.4 rad/s case. Therefore, the divergence observed in Fig. 14 is beneficial for deep stall recovery. It can also be inferred that an aircraft with more serious deep stall characteristics may not recover if the pilot relies on the linear resonance frequency (that turns out to be stable on the nonlinear Bode plot). To prevent this, nonlinear frequency analysis should be employed to identify the unstable (diverging) frequencies that guarantee large-amplitude oscillations that contribute to a successful recovery.

The proposed method of destabilising the deep stall trim point via harmonic forcing is effective because there is always a region of unstable trimmed (equilibrium) conditions across the angles of attack range between the deep stall and normal flight regions. This can be verified in the  $C_m$  plot (Fig. 6) as well as the unforced bifurcation diagram (Fig. 5), both of which show that the aircraft is unstable between 9° and 30° angles of attack. This type of pitching moment trend is a characteristic of deep stall in general and T-tailed aircraft in particular. When the elevator travels across these unstable regions under the harmonic oscillatory input, it becomes possible to induce a large-amplitude oscillation due to the existence of the unstable trim points mentioned. The nonlinear frequency response approach, derived from numerical bifurcation analysis, allows us to identify the forcing parameters that can excite this resonance and increase the chance of a successful recovery.

Regarding the practical aspects our results presented so far, the resonance frequency of 0.40 rad/s equals 0.064 Hz, which demands a very slow elevator travel rate of no more than 8 deg/s. In case the pitch pumping frequency is higher and involves high risk of encountering actuator rate limiting, nonlinear frequency analysis can still account for rate saturation as demonstrated in [17].

We now compare the pitch rocking method with the other alternative of invoking a lateral control input (aileron in this case) to roll the aircraft about the body axis. In principle, a body-axis roll at high angles of attack will convert  $\alpha$  into sideslip  $\beta$  due to kinematic coupling. This may help reduce  $\alpha$  to regain control of the aircraft, but at a cost of potentially invoking large lateral-directional motions that can take the aircraft into an upset/loss-of-control situation. To demonstrate, a recovery is now attempted by rolling the deep-stalled eighth-order aircraft model (containing lateral-directional dynamics) using maximum aileron ( $\delta_a = 25^\circ$ ). Figure 16 compares the responses using two different elevator positions: neutral ( $\delta_e = 0^\circ$ ) and full nose-down ( $\delta_e = 20^\circ$ ). The former enters a stable limit-cycle at high  $\alpha$ , thereby showing no signs of recovery. On the other hand, combining the nose-down and rolling inputs will bring the angle-of-attack down to the normal range after around 30 seconds. Although this manoeuvre successfully reduces  $\alpha$  in a similar time frame to the pitch rocking example in Fig. 15, the aircraft is now in an upset condition involving large bank and sideslip angles ( $\phi$  approaching  $-90^\circ$  and  $\beta$  around  $-50^\circ$ ), thereby making it more susceptible to entering a spin, autorotation, or other loss-of-control situations. This lateral-directional approach also incurs significant height loss, making it more dangerous compared to the proposed pitch rocking method.

#### 4.4 Influence of aerodynamic asymmetries

All real aircraft contain aerodynamic asymmetries, especially at high angles of attack. Therefore, it is important to verify the dynamic recovery technique in the presence of these features. The analysis now considers the eighth-order (6 degrees of freedom) asymmetric GTT model. The asymmetric data was compiled by NASA from wind tunnel tests in the NASA Langley Research Center 12-Foot Low-Speed Tunnel (12-Foot LST) and the Boeing North American Aviation Research Tunnel (NAART), yielding two separate sets of data with the latter having smaller magnitude asymmetries. Data from the NAART is considered more indicative and is used in this section, mainly because no detailed investigation into aerodynamic asymmetry of this type of aircraft has been conducted. The contribution of asymmetries to the total rolling moment  $C_l$ , yawing moment  $C_n$ , and side force  $C_y$  are shown in Fig. 17. Due to their

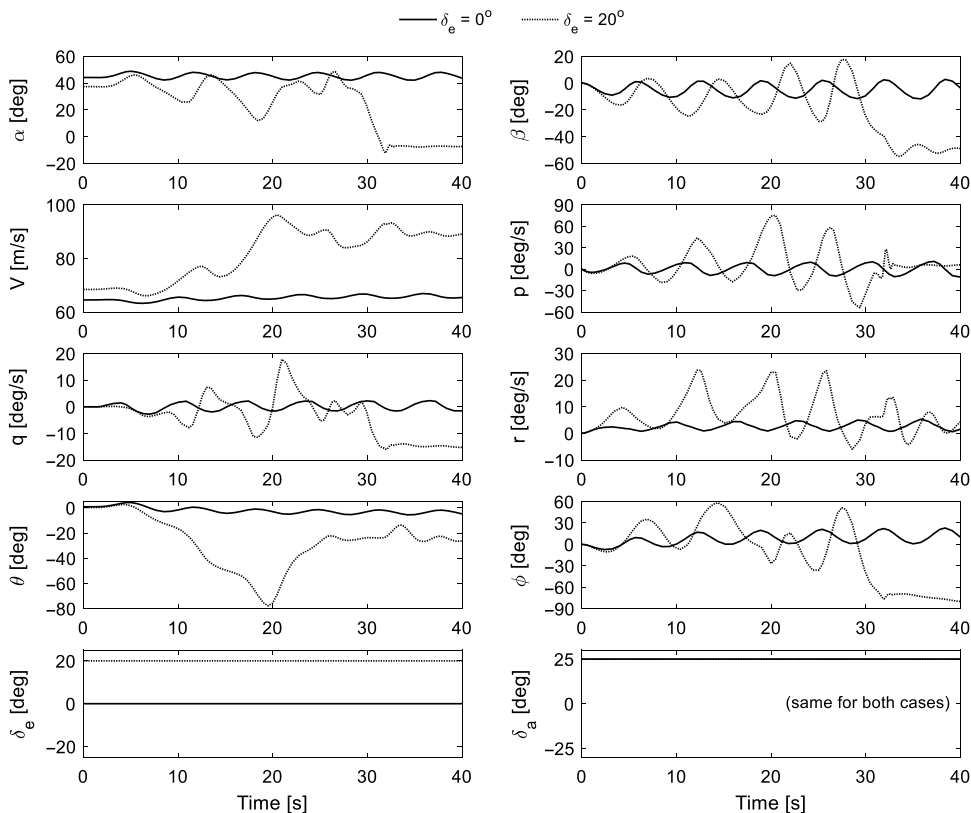


Figure 16. Eighth-order time simulation at full left roll aileron ( $\delta_a = 25^\circ$ ).

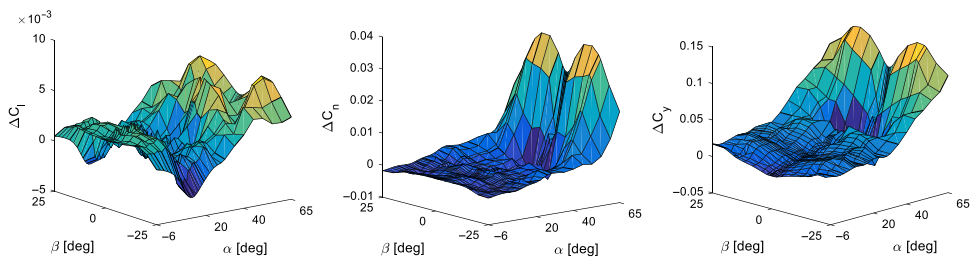
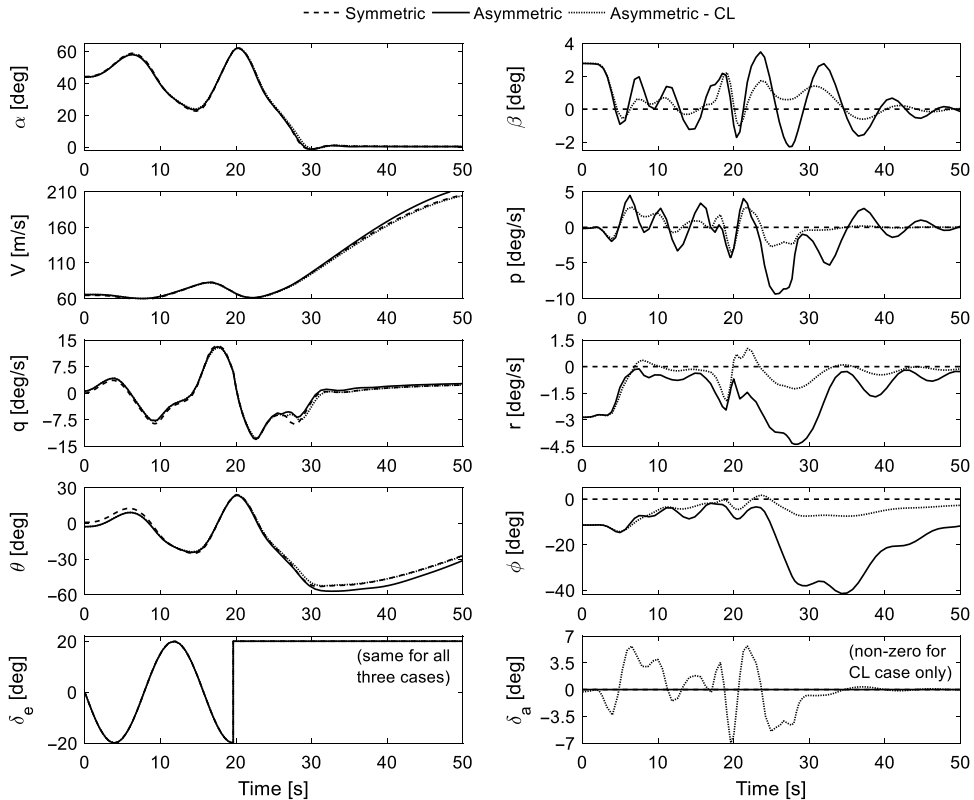


Figure 17. Asymmetric aerodynamic coefficients.

presence, the flight condition at deep stall for zero elevator, aileron, and rudder inputs becomes  $\alpha = 44^\circ$ ,  $V = 66 \text{ m/s}$ ,  $q = 0.58^\circ/\text{s}$ ,  $\theta = -2.7^\circ$ ,  $\beta = 2.8^\circ$ ,  $p = -0.14^\circ/\text{s}$ ,  $r = -2.86^\circ/\text{s}$ , and  $\phi = -11.4^\circ$ .

In this section, the following three different implementations of the eighth-order model are considered:

- Symmetric: contains no aerodynamic asymmetries. The responses are equivalent to that of the 4<sup>th</sup>-order responses above as long as no lateral-directional input or perturbation is given. This model is considered here for reference only.
- Asymmetric: contains aerodynamic asymmetries using the NAART dataset.



**Figure 18.** Comparing deep stall recovery on the eighth-order models.

- Asymmetric – CL: same as above but with the addition of roll rate feedback to the aileron. The addition of a roll damping controller allows us to ascertain that it is possible to overcome aerodynamic asymmetries using conventional control methods, which is important for a safe recovery.

The recovery manoeuvre using elevator movement as shown in Fig. 15 (oscillations at 0.40 rad/s) is now tested on these three eighth-order models. Their responses are shown in Fig. 18, noting that all longitudinal variables are placed in the first column. It can be seen that there is minimal variation in the longitudinal responses in all three cases, indicating that our proposed deep stall recovery manoeuvre is effective even in the presence of aerodynamic asymmetries. The main differences are in the lateral-directional responses shown in the second column. Specifically:

- The symmetric model contains no lateral-directional motions (as expected).
- The open-loop asymmetric model invokes large bank angles ( $\phi$ ) that exceeded  $40^\circ$  during the manoeuvre. Notably,  $\phi$  did not vary much during the initial stick pumping phase, but then increased rapidly when the nose-down push was initiated at the 19.6s mark.
- The roll-damping controller is very effective at reducing bank angle, and accordingly other lateral-directional variables as well. In this example, the proportional stability-augmentation gain was set to 2.0. This resulted in aileron movements that can be considered reasonable as seen in the  $\delta_a$  time history, showing a  $-7^\circ$  peak in travel and  $10^\circ/\text{s}$  peak in rate. We can therefore conclude that the control input required to keep the wing close to level throughout the manoeuvre can be achieved, whether through the use of a controller or potentially via pilot input.

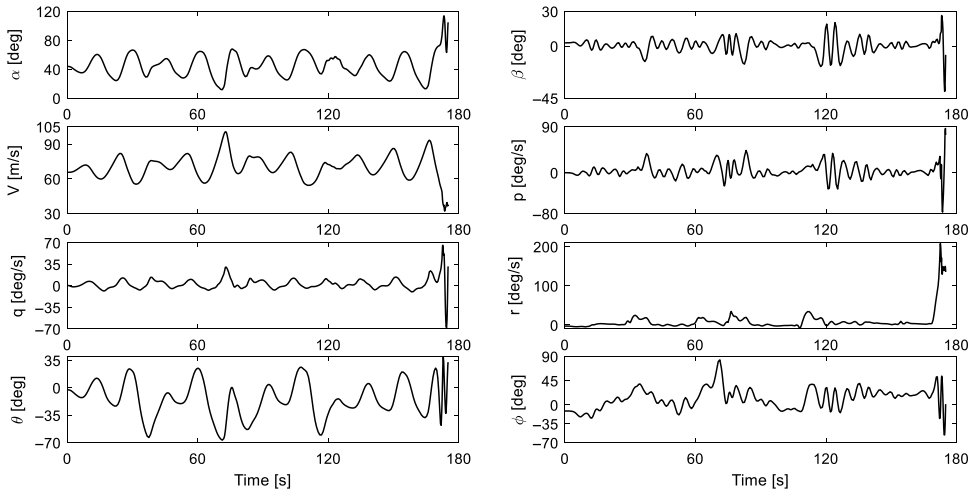


Figure 19. Sinusoidal elevator forcing at 0.40 rad/s – open-loop asymmetric model.

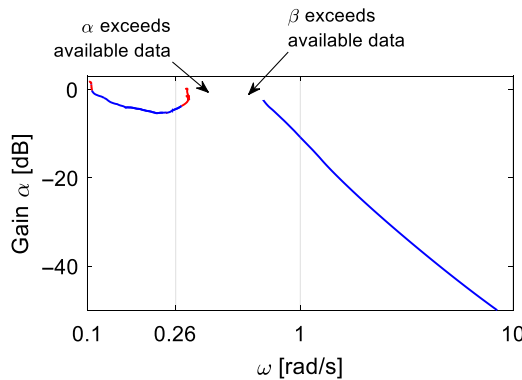
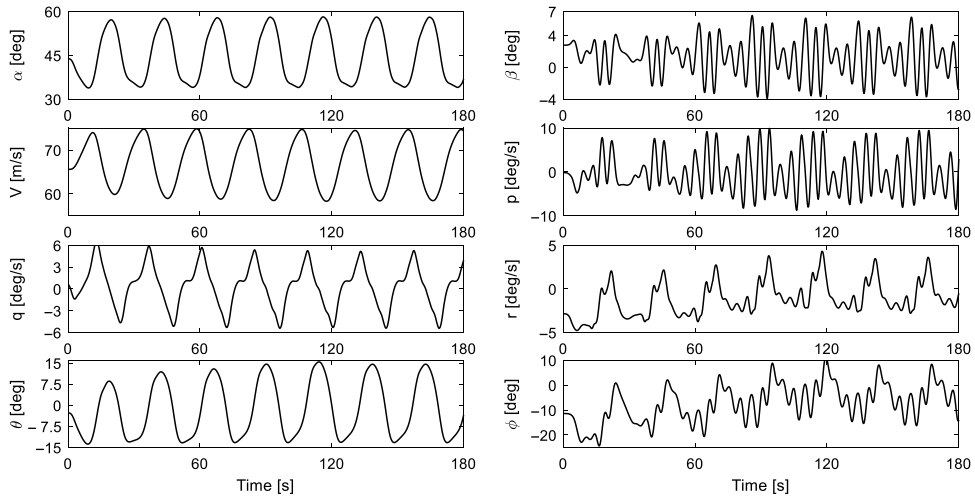


Figure 20. Partial  $\delta_e$ -to- $\alpha$  frequency response of the open-loop asymmetric implementation.

Nonlinear frequency analysis is unfortunately no longer effective in this instance. Since the nonlinear Bode plot only shows the final steady-state response and provides no indication of the transient dynamics, the unstable solutions may reflect a divergent response involving large lateral-directional oscillations, which is detrimental for a safe recovery. This can be illustrated by continuing the stick-pumping at 0.40 rad/s on the open-loop asymmetric model as shown in Fig. 18 but without the nose-down push, resulting in the response in Fig. 19. It can be seen that the dynamics is complex and involves large lateral-directional components. The continuation algorithm will attempt to solve for these responses, which is numerically intense and may not yield useful information.

We were able to partially generate the frequency response of the open-loop asymmetric model as shown in Fig. 20. The diagram’s shape suggests that resonance still occurs around 0.40 rad/s as seen in the 4<sup>th</sup>-order analysis. However, solutions around the resonance region exceed the available aerodynamic data and involve heavy coupling between longitudinal and lateral-directional motions. Although spline extrapolation can be used to solve beyond the existing data, this procedure is numerically intense and may not yield valid results. Therefore, we decided not to pursue nonlinear frequency analysis on the eighth-order model.

Figure 21 further illustrates the difficulties encountered when using nonlinear frequency analysis in the presence of lateral-directional coupling due to aerodynamic asymmetries. Although the partial



**Figure 21.** *Open-loop asymmetric forced response at  $\omega = 0.26$  rad/s.*

nonlinear Bode plot correctly predicted that 0.26 rad/s forced response is stable as shown in Fig. 21, the dynamics is very complex and involves large lateral-directional components. Furthermore, we have demonstrated that the pilot should initiate the nose-down push after around 1.5 forcing cycles. This is too early for the forced response to converge to its final steady-state solutions as predicted by the nonlinear asymmetric frequency analysis. Therefore, the use of continuation in the presence of aerodynamic asymmetries is unnecessary for deriving a deep stall recovery manoeuvre for this aircraft model.

To sum up, the pitch rocking technique remains effective for deep stall recovery even in the presence of aerodynamic asymmetries, although an upset/loss-of-control incident is possible if the lateral-directional motions is not minimised. This can be prevented by damping the rolling (and potentially also yawing) motions throughout the manoeuvre. In the GTT example considered, the stability augmentation controller successfully stabilised the aircraft while also showing that the aileron movement required to keep the wing close to level is reasonable. Such a control input can therefore be expected from a pilot doing manual flying, at least after the stick-pumping phase.

## 5.0 Conclusion

In this paper, we have shown that bifurcation methods implemented in the form of nonlinear frequency analysis can facilitate a systematic study to identify possible deep stall recovery manoeuvres in a T-tailed aircraft. Despite the existence of the locked-in deep stall at full nose-down elevator, it is still possible to initiate recovery by forcing the pitch control device at one of the nonlinear resonant frequencies. This manoeuvre destabilises the statically stable trim point via a divergent pitch oscillation, which enables the pilot to rock the aircraft out of a potentially unrecoverable deep stall without invoking large lateral-directional motions that can lead to an upset and loss-of-control situation. The forcing frequencies that result in these divergent responses can be identified using nonlinear frequency analysis, and were found to be slightly lower than the resonance frequency predicted by classical methods. In other words, the resonance frequency predicted by linear methods is insufficiently close to the true resonance peak, and this can prevent a successful deep stall recovery. These results also present a rare example of unstable (divergent) solutions being beneficial in the context of flight dynamics and control. Furthermore, the pitch rocking method is safer than recovery methods that induce lateral-directional motions, which come with high risk of triggering an upset condition. The presence of aerodynamic asymmetries does not preclude recovery because the aircraft considered here has enough control power to counteract the

lateral-directional motions. However, aerodynamic asymmetries do reduce the effectiveness of the non-linear frequency analysis method. Our approach for deriving a dynamic deep stall recovery manoeuvre is therefore limited to fourth-order longitudinal analysis.

It was also found that at high angles of attack, the frequency separation between the conventional short-period and phugoid modes is significantly reduced, leading to non-conventional dynamics that resemble only one single mode. This further highlights the nonlinear nature of high angles of attack behaviours that may have hindered previous studies of dynamic deep stall recovery, most of which were also limited to empirical methods. The proposed nonlinear frequency approach provides not only a systematic study of dynamic deep stall recovery, but also expands the nonlinear analysis toolbox to account for both stationary and non-stationary nonlinearities.

**Acknowledgements.** The first author is partially supported by the University of Bristol's Alumni Grant. We are grateful to NASA Langley Research Center, specifically Kevin Cunningham and Gautam Shah, for providing the GTT model.

## References

- [1] Trubshaw, E.B. Low speed handling with special reference to the super stall, *Aeronaut. J.*, 1966, **70**, (667), pp 695–704.
- [2] Iloputaife, O.I. Design of deep stall protection for the C-17A, *J. Guid. Control Dyn.*, 1997, **20**, (4), pp 760–767.
- [3] Nguyen, L.T., Ogburn, M.E., Gilbert, W.P., Kibler, K.S., Brown, P.W. and Deal, P.L. Simulator Study of Stall/Post-Stall Characteristics of a Fighter Airplane with Relaxed Longitudinal Static Stability, *NASA Technical Paper 1538*. NASA, Langley Research Center, Hampton, Virginia, 1979.
- [4] Prechtl, R. Russ at F 16 CTF 95 96. <https://www.youtube.com/watch?v=qg1Ojydzv8U> [retrieved 27 December 2021].
- [5] Avanzini, G. and Matteis, G.D. Bifurcation analysis of a highly augmented aircraft model, *J. Guid. Control Dyn.*, 1997, **20**, (4), pp 754–759.
- [6] Gousman, K., Loschke, R., Rooney, R. and Juang, J. Aircraft deep stall analysis and recovery, *18th Atmospheric Flight Mechanics Conference*, New Orleans, LA, 1991.
- [7] Montgomery, R.C. and Moul, M.T. Analysis of deep-stall characteristics of T-tailed aircraft configurations and some recovery procedures, *J. Aircr.*, 1966, **3**, (6), pp 562–566.
- [8] Kolb, S., Hétru, L., Faure, T.M. and Montagnier, O. Nonlinear analysis and control of an aircraft in the neighbourhood of deep stall, *ICNPAA 2016 World Congress*, La Rochelle, France, 2016.
- [9] Wu, D., Chen, M. and Ye, H. Analysis and recovery of aircraft deep-stall phenomena using bifurcation analysis, *IEEE Access*, 2020, **8**, pp 29319–29333.
- [10] Evangelou, L.D., Self, A.W., Allen, J.E. and Lo, S. Trimmed deep stall on the F-16 Fighting Falcon, *Aeronaut. J.*, 2001, **105**, (1054), pp 679–683.
- [11] Nguyen, D.H., Lowenberg, M.H. and Neild, S.A. Analysing dynamic deep stall recovery using a nonlinear frequency approach, *Nonlin. Dyn.* doi: [10.1007/s11071-022-07283-z](https://doi.org/10.1007/s11071-022-07283-z).
- [12] Carroll, J.V. and Mehra, R.K. Bifurcation analysis of nonlinear aircraft dynamics, *J. Guid. Control Dyn.*, 1982, **5**, (5), pp 529–536.
- [13] Goman, M.G., Zagainov, G.I. and Khramtsovsky, A.V. Application of bifurcation methods to nonlinear flight dynamics problems, *Prog. Aerosp. Sci.*, 1997, **33**, (9–10), pp 539–586.
- [14] Richardson, T., Lowenberg, M., di Bernardo, M. and Charles, G. Design of a gain-scheduled flight control system using bifurcation analysis, *J. Guid. Control Dyn.*, 2006, **29**, (2), pp 444–453.
- [15] Gill, S.J., Lowenberg, M.H., Neild, S.A., Crespo, L.G. and Krauskopf, B. Impact of controller delays on the nonlinear dynamics of remotely piloted aircraft, *J. Guid. Control Dyn.*, 2016, **39**, (2), pp 292–300.
- [16] Nguyen, D.H., Lowenberg, M.H. and Neild, S.A. Frequency-domain bifurcation analysis of a nonlinear flight dynamics model, *J. Guid. Control Dyn.*, 2021, **44**, (1), pp 138–150.
- [17] Nguyen, D.H., Lowenberg, M.H. and Neild, S.A. Effect of actuator saturation on pilot-induced oscillation: a nonlinear bifurcation analysis, *J. Guid. Control Dyn.*, 2021, **44**, (5), pp 1018–1026.
- [18] Gill, S.J., Lowenberg, M.H., Neild, S.A., Krauskopf, B., Puyou, G. and Coetzee, E. Upset dynamics of an airliner model: A nonlinear bifurcation analysis, *J. Aircr.*, 2013, **50**, (6), pp 1832–1842.
- [19] Belcastro, C.M., Foster, J., Newman, R.L., Groff, L., Crider, D.A. and Klyde, D.H. Preliminary analysis of aircraft loss of control accidents: Worst case precursor combinations and temporal sequencing, *AIAA Guidance, Navigation, and Control Conference*, National Harbor, Maryland, 2014.
- [20] Thomas, P.R., Bullock, S., Bhandari, U. and Richardson, T.S. Fixed-wing approach techniques for complex environments, *Aeronaut. J.*, 2015, **119**, (1218), pp 999–1016.
- [21] Cunis, T., Condomines, J.-P. and Burlion, L. Sum-of-squares flight control synthesis for deep-stall recovery, *J. Guid. Control Dyn.*, 2020, **43**, (8), pp 1498–1511.
- [22] Cunis, T., Condomines, J.-P., Burlion, L. and Cour-Harbo, A.L. Dynamic stability analysis of aircraft flight in deep stall, *J. Aircr.*, 2020, **57**, (1), pp 143–155.
- [23] Coetzee, E., Krauskopf, B. and Lowenberg, M.H. The dynamical systems toolbox: Integrating AUTO into Matlab, *16th US National Congress of Theoretical and Applied Mechanics*, State College, PA, 2010.

- [24] Doedel, E.J. AUTO-07P, Continuation and Bifurcation Software for Ordinary Differential Equations, Ver. 07P, <http://www.macs.hw.ac.uk/~gabriel/auto07/auto.html> [retrieved 8 April 2021].
- [25] Cunningham, K., Shah, G.H., Frink, N.T., McMillin, S.N., Murphy, P.C., Brown, F.R., Hayes, P.J., Shweyk, K.M. and Nayani, S.N. Preliminary test results for stability and control characteristics of a generic T-tail transport airplane at high angle of attack, *2018 AIAA Atmospheric Flight Mechanics Conference*, Kissimmee, Florida, 2018.
- [26] Cunningham, K., Shah, G.H., Hill, M.A., Pickering, B.P., Litt, J.S. and Norin, S. A Generic T-tail transport airplane simulation for high-angle-of-attack dynamics modeling investigations, *2018 AIAA Modeling and Simulation Technologies Conference*, Kissimmee, Florida, 2018.
- [27] Cunningham, K., Shah, G.H., Murphy, P.C., Hill, M.A. and Pickering, B. Pilot sensitivity to simulator flight dynamics model formulation for stall training, *AIAA Scitech 2019 Forum*, San Diego, California, 2019.
- [28] Doedel, E., Keller, H.B. and Kernevez, J.P. Numerical analysis and control of bifurcation problems (I): Bifurcation in finite dimensions, *Int. J. Bifurc. Chaos*, 1991, **01**, (03), pp 493–520.
- [29] Doedel, E., Keller, H.B. and Kernevez, J.P. Numerical analysis and control of bifurcation problems (II): Bifurcation in infinite dimensions, *Int. J. Bifurc. Chaos*, 1991, **01**, (04), pp 745–772.
- [30] Perez, M.M. and Lowenberg, M.H. Eigenvector similarity metrics for the identification and quantitative study of aircraft dynamic modes, *AIAA Scitech 2021 Forum*, online event, 2021.

## APPENDIX

### A1. LINEAR APPROXIMATIONS

The linear state-space models and transfer functions for the aircraft trimmed in normal flight and deep stall are presented in this section. In both cases, the following flight conditions apply: full nose-up tailplane ( $-10^\circ$ ),  $T = 0$  N, and  $cg = 40\%$  MAC. The state and input vectors are  $\mathbf{x} = [\alpha, V, q, \theta]^T$  and  $\mathbf{u} = \delta_e$ . Note that  $\alpha$ ,  $q$ , and  $\theta$  have units rad/s or rad in the state-space matrices.

#### Low- $\alpha$ flight:

$$\delta_e = 17^\circ, \alpha = 4.86 \text{ deg}, V = 107.4 \text{ m/s}, q = 0 \text{ deg/s}, \theta = -0.22 \text{ deg}$$

$$A = \begin{bmatrix} -0.6609 & -0.0017 & 0.9502 & 0.0081 \\ 2.8242 & -0.0162 & -0.0744 & -9.7715 \\ -1.6463 & -8.083e^{-7} & -0.4654 & 0 \\ 0 & 0 & 1 & 0 \end{bmatrix} \quad B = \begin{bmatrix} -0.0008974 \\ -0.0099916 \\ -0.0235426 \\ 0 \end{bmatrix}$$

$$C = \begin{bmatrix} 1 & 0 & 0 & 0 \\ 0 & 1 & 0 & 0 \\ 0 & 0 & 1 & 0 \\ 0 & 0 & 0 & 1 \end{bmatrix} \quad D = \begin{bmatrix} 0 \\ 0 \\ 0 \\ 0 \end{bmatrix}$$

$$\frac{\alpha(s)}{\delta_e(s)} = \frac{-0.051416 (s + 25.37) (s^2 + 0.02366s + 0.01726)}{(s^2 + 0.01579s + 0.01475) (s^2 + 1.127s + 1.862)} \quad \left( \frac{\text{deg}}{\text{deg}} \right)$$

$$\frac{V(s)}{\delta_e(s)} = \frac{-0.0099916 (s - 3.739) (s + 4.035) (s + 0.9084)}{(s^2 + 0.01579s + 0.01475) (s^2 + 1.127s + 1.862)} \quad \left( \frac{\text{m/s}}{\text{deg}} \right)$$

$$\frac{q(s)}{\delta_e(s)} = \frac{-1.3489s (s + 0.5877) (s + 0.02662)}{(s^2 + 0.01579s + 0.01475) (s^2 + 1.127s + 1.862)} \quad \left( \frac{\text{deg/s}}{\text{deg}} \right)$$

$$\frac{\theta(s)}{\delta_e(s)} = \frac{-1.3489 (s + 0.5877) (s + 0.02662)}{(s^2 + 0.01579s + 0.01475) (s^2 + 1.127s + 1.862)} \quad \left( \frac{\text{deg}}{\text{deg}} \right)$$

**Deep stall:**

$\delta_e = 0^\circ, \alpha = 44.2 \text{ deg}, V = 64.5 \text{ m/s}, q = 0 \text{ deg/s}, \theta = 0.87 \text{ deg}$

$$A = \begin{bmatrix} -0.13858 & -0.00343 & 0.92943 & 0.10426 \\ -7.14144 & -0.20869 & -4.27044 & -7.13799 \\ -0.62887 & 2.74314e^{-6} & -0.34515 & -6.30705 \\ 0 & 0 & 1 & 0 \end{bmatrix} \quad B = \begin{bmatrix} -0.00024411 \\ -0.011471 \\ -0.0035998 \\ 0 \end{bmatrix}$$

$$C = \begin{bmatrix} 1 & 0 & 0 & 0 \\ 0 & 1 & 0 & 0 \\ 0 & 0 & 1 & 0 \\ 0 & 0 & 0 & 1 \end{bmatrix} \quad D = \begin{bmatrix} 0 \\ 0 \\ 0 \\ 0 \end{bmatrix}$$

$$\frac{\alpha(s)}{\delta_e(s)} = \frac{-0.013986 (s + 13.77) (s^2 + 0.3328s + 0.04953)}{(s^2 + 0.3345s + 0.05439) (s^2 + 0.3579s + 0.5347)} \quad \left( \frac{\text{deg}}{\text{deg}} \right)$$

$$\frac{V(s)}{\delta_e(s)} = \frac{-0.011471 (s - 2.572) (s + 1.461) (s + 0.1019)}{(s^2 + 0.3345s + 0.05439) (s^2 + 0.3579s + 0.5347)} \quad \left( \frac{\text{m/s}}{\text{deg}} \right)$$

$$\frac{q(s)}{\delta_e(s)} = \frac{-0.20625 s (s + 0.2965) (s + 0.008109)}{(s^2 + 0.3345s + 0.05439) (s^2 + 0.3579s + 0.5347)} \quad \left( \frac{\text{deg/s}}{\text{deg}} \right)$$

$$\frac{\theta(s)}{\delta_e(s)} = \frac{-0.20625 (s + 0.2965) (s + 0.008109)}{(s^2 + 0.3345s + 0.05439) (s^2 + 0.3579s + 0.5347)} \quad \left( \frac{\text{deg}}{\text{deg}} \right)$$

**A2. DATA FOR THE FOURTH-ORDER LONGITUDINAL GTT**

	$C_{x_0}(\alpha)$	$C_{z_0}(\alpha)$	$C_{m_0}(\alpha)$	$C_{x_2}(\alpha)$	$C_{z_2}(\alpha)$	$C_{m_2}(\alpha)$
$\alpha$ (deg) -8	0.001756	0.573304	0.432268	-	-	-
-4	-0.03202	0.158374	0.261432	0.681504	-13.8149	-40.643
0	-0.03678	-0.25651	0.097101	-0.37529	-18.1738	-43.356
2	-	-	-	0.545445	-17.2006	-
4	-0.00629	-0.62505	-0.0754	1.937841	-17.6061	-41.181
6	0.01381	-0.77965	-0.18194	1.31688	-31.494	-
8	0.022591	-0.92885	-0.28825	4.707579	-40.767	-34.745
9	-	-	-0.32747	-	-	-
10	0.024658	-1.02196	-0.31196	8.902535	-58.0184	-69.126
11	0.02303	-1.05948	-0.32356	-	-	-
12	0.017965	-1.07378	-0.33825	10.38419	-67.2923	-96.728
13	0.01317	-1.09069	-0.35346	-	-	-
14	0.009066	-1.10536	-0.36577	6.313846	-64.1955	-114.97
15	0.002488	-1.11635	-0.37268	-	-	-
16	-0.00356	-1.12605	-0.21655	5.502465	-69.2124	-112.37
17	-0.00821	-1.13737	-0.16443	-	-	-
18	-0.01083	-1.15242	-0.1382	5.978998	-64.8436	-25.745

	$C_{x_0}(\alpha)$	$C_{z_0}(\alpha)$	$C_{m_0}(\alpha)$	$C_{x_2}(\alpha)$	$C_{z_2}(\alpha)$	$C_{m_2}(\alpha)$
19	-0.01369	-1.15662	-0.12153	-	-	-
20	-0.01642	-1.17081	-0.13459	1.620688	-47.6716	-0.43262
22	-0.02218	-1.16413	-0.1816	0.363719	-30.5866	-16.712
24	-0.02217	-1.2197	-0.18915	1.976721	-31.3621	-43.392
26	-0.01945	-1.29772	-0.1872	0.480189	-28.9413	-47.317
28	-0.01606	-1.35679	-0.19594	-1.23985	-31.8403	-44.361
30	-0.01263	-1.44425	-0.21354	0.52692	-33.8075	-45.17
35	-0.00051	-1.61095	-0.24148	0.300702	-37.0869	-57.502
40	0.008251	-1.7952	-0.33638	1.00132	-42.515	-52.381
45	0.019853	-1.97111	-0.55827	-	-	-
50	0.035626	-2.15076	-0.74842	0.547605	-50.4169	-50.576
55	0.047189	-2.18336	-0.83617	-	-	-
60	0.064759	-2.26355	-0.90179	-1.5126	-38.7345	-67.185

		$\delta_e$ (deg)				
$C_{x_1}(\alpha, \delta_e)$		-20	-10	0	10	20
$\alpha$ (deg)	-8	-0.06694	-0.04867	-0.03525	-0.02391	-0.01908
	-4	-0.0557	-0.03486	-0.02201	-0.01002	-0.00647
	0	-0.04621	-0.02518	-0.01148	-0.00356	-0.0049
	4	-0.03592	-0.02016	-0.01061	-0.00464	-0.00584
	6	-0.0372	-0.02266	-0.01149	-0.00333	-0.00462
	8	-0.03848	-0.02326	-0.01164	-0.00271	-0.00438
	10	-0.03882	-0.02324	-0.0122	-0.00341	-0.003
	11	-0.03705	-0.02166	-0.00926	-0.00115	-0.00204
	12	-0.03874	-0.02219	-0.00951	-0.00158	-0.00338
	13	-0.03884	-0.02237	-0.01003	-0.00208	-0.00287
	14	-0.03977	-0.02331	-0.01009	-0.00223	-0.00403
	15	-0.03936	-0.02339	-0.00979	-0.00258	-0.00435
	16	-0.03902	-0.02328	-0.00957	-0.00332	-0.00481
	17	-0.03965	-0.0227	-0.01002	-0.00189	-0.00354
	18	-0.03871	-0.02225	-0.0101	-0.00253	-0.00339
	19	-0.03724	-0.02021	-0.00849	-0.00201	-0.00251
	20	-0.03614	-0.02064	-0.00782	-0.00151	-0.00102
	22	-0.0311	-0.01724	-0.00548	0.001833	0.002747
	24	-0.02608	-0.01278	-0.00243	0.003651	0.004542
	26	-0.02065	-0.00976	-0.00057	0.003944	0.004448
	28	-0.01699	-0.00755	0.000428	0.004406	0.004747
	30	-0.01356	-0.00663	0.000938	0.004875	0.004046
	35	-0.01045	-0.00482	0.000725	0.00465	0.003494
	40	-0.00699	-0.00189	0.004697	0.006261	0.004732
	45	-0.00706	0.001473	0.011849	0.012503	0.010597
	50	-0.00328	0.006448	0.017819	0.020957	0.014611
	55	0.006206	0.016745	0.029021	0.026619	0.020563
	60	0.014154	0.023574	0.030077	0.027793	0.018647

$C_{z_1}(\alpha, \delta_e)$		$\delta_e$ (deg)				
		-20	-10	0	10	20
$\alpha$ (deg)	-8	0.132483	0.109126	0.080109	0.034874	-0.03212
	-4	0.158259	0.131368	0.095109	0.041325	-0.0344
	0	0.211822	0.186351	0.13575	0.056794	-0.02816
	4	0.259968	0.220388	0.155453	0.065812	-0.00213
	6	0.263041	0.211611	0.14721	0.048612	-0.01741
	8	0.260209	0.22054	0.157436	0.056434	-0.00748
	10	0.26989	0.219953	0.149982	0.068683	-0.02324
	11	0.268262	0.21701	0.132912	0.05184	-0.01867
	12	0.262347	0.199729	0.130679	0.05542	-0.01271
	13	0.264113	0.206197	0.126217	0.050133	-0.02485
	14	0.244049	0.197291	0.132894	0.04268	-0.03004
	15	0.24873	0.192789	0.13868	0.033549	-0.02258
	16	0.243716	0.190645	0.133882	0.042625	-0.02503
	17	0.235976	0.191473	0.123993	0.042329	-0.03392
	18	0.2319	0.188976	0.118089	0.055378	-0.02209
	19	0.215836	0.179823	0.117448	0.049292	-0.02995
	20	0.230695	0.182805	0.135622	0.072027	-0.02192
	22	0.202552	0.146864	0.094765	0.032169	-0.01676
	24	0.176827	0.138095	0.098046	0.035512	-0.01218
	26	0.170254	0.141196	0.104579	0.032826	-0.01391
	28	0.127114	0.128839	0.087652	0.019884	-0.01556
	30	0.145601	0.109992	0.072914	0.060579	0.022069
	35	0.127895	0.087692	0.051448	0.039069	0.017377
	40	0.135045	0.091388	0.070557	0.03279	0.028652
	45	0.146468	0.120365	0.055801	0.043267	-0.01268
	50	0.149586	0.165258	0.08059	0.006591	0.043287
	55	0.127524	0.109323	0.007271	0.010296	-0.03288
	60	0.097676	0.0627	0.037962	-0.00345	-0.00168

$C_{m_1}(\alpha, \delta_e)$		$\delta_e$ (deg)				
		-20	-10	0	10	20
$\alpha$ (deg)	-8	0.599929	0.496285	0.360396	0.165401	-0.09051
	-4	0.727396	0.6063	0.453146	0.209627	-0.11065
	0	0.882632	0.737964	0.531845	0.204653	-0.11927
	4	1.019251	0.842174	0.581101	0.228223	-0.07715
	6	1.052524	0.887267	0.602272	0.227272	-0.06158
	8	1.091908	0.91249	0.605274	0.230106	-0.04692
	10	1.089233	0.915819	0.613027	0.226843	-0.04188
	11	1.095252	0.91482	0.618201	0.220547	-0.04392
	12	1.097219	0.915501	0.611368	0.2171	-0.04082
	13	1.090578	0.907631	0.612453	0.216307	-0.04625
	14	1.100774	0.91114	0.600114	0.211275	-0.05055

$C_{m_1}(\alpha, \delta_e)$	$\delta_e$ (deg)				
	-20	-10	0	10	20
16	1.055232	0.857304	0.561339	0.191742	-0.08064
17	1.042249	0.830016	0.545924	0.186884	-0.09103
18	1.017316	0.799976	0.526382	0.184602	-0.09576
19	0.995487	0.769238	0.504485	0.180434	-0.09639
20	0.955327	0.735492	0.482036	0.179241	-0.09046
22	0.854531	0.647987	0.429445	0.160814	-0.07753
24	0.762102	0.563335	0.37125	0.143026	-0.06387
26	0.662591	0.489183	0.334354	0.130198	-0.04861
28	0.589133	0.434342	0.286587	0.121218	-0.02999
30	0.508876	0.392271	0.273722	0.126029	0.00255
35	0.409975	0.313753	0.231067	0.118764	0.025011
40	0.407095	0.302035	0.233108	0.110704	0.045697
45	0.512455	0.374348	0.240365	0.10647	1.32E-05
50	0.564861	0.377184	0.231874	0.062937	-0.02644
55	0.513756	0.330379	0.147294	0.030879	-0.05165
60	0.43169	0.267761	0.144154	0.030797	-0.01758